ACS APPLIED MATERIALS & INTERFACES

www.acsami.org

Research Article

Engineering Interface Defects and Interdiffusion at the Degenerate Conductive In_2O_3/Al_2O_3 Interface for Stable Electrodes in a Saline Solution

Zetao Zhu,* Takao Yasui,* Xixi Zhao, Quanli Liu, Shu Morita, Yan Li, Akira Yonezu, Kazuki Nagashima, Tsunaki Takahashi, Minoru Osada, Ryotaro Matsuda, Takeshi Yanagida, and Yoshinobu Baba*

Cite This: *ACS Appl. Mater. Interfaces* 2023, 15, 36866−36876

Read Online

ACCESS | Metrics & More | Article Recommendations | Supporting Information

ABSTRACT: A low-temperature Al_2O_3 deposition process provides a simplified method to form a conductive two-dimensional electron gas (2DEG) at the metal oxide/Al_2O_3 heterointerface. However, the impact of key factors of the interface defects and cation interdiffusion on the interface is still not well understood. Furthermore, there is still a blank space in terms of applications that go beyond the understanding of the interface's electrical conductivity. In this work, we carried out a systematic experimental study by oxygen plasma pretreatment and thermal annealing post-treatment to study the impact of interface defects and cation interdiffusion at the In_2O_3/Al_2O_3 interface on the electrical conductance, respectively. Combining the trends in electrical conductance with the structural characteristics, we found that building a sharp interface with a high concentration of interface defects provides a reliable approach to producing such a conductive interface. After applying this conductive interface as electrodes for fabricating a field-effect transistor (FET) device, we found that this interface electrode exhibited ultrastability in phosphate-buffered saline (PBS), a commonly used biological saline solution. This study provides new insights into the formation of conductive 2DEGs at metal oxide/Al_2O_3 interfaces and lays the foundation for further applications as electrodes in bioelectronic devices.

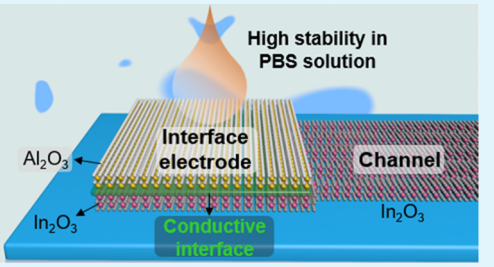

KEYWORDS: *2DEG, conductive interface, interface engineering, interface electrode, stability in biological saline*

1. INTRODUCTION

The heterointerfaces between two different insulating oxide materials can exhibit interfacial superconductivity different from that of either component, which is attributed to the formation of a conductive two-dimensional electron gas (2DEG) at the interface.[1−5] Experimental and theoretical studies of the 2DEG interface between two oxide insulators, $LaAlO_3$ (LAO) and $SrTiO_3$ (STO), have revealed intriguing physical phenomena, such as superconductivity,[6−8] magnetic interaction,[9−11] field-tunable metal−insulator transition,[3,12] and quantized transport.[13,14] However, the 2DEG formed at the epitaxial interface of the LAO/STO requires harsh fabrication conditions, for example, LAO layers must be grown on Ti-terminated STO single-crystalline substrates at high temperatures by pulsed laser deposition or molecular beam epitaxy.[15−20] There are other examples: the conductivity[21−25] or mobility[26−30] in many functional electronic devices should be controlled by engineering processes, such as impurity doping;[31,32] and lithography and etching processes are required for the device fabrications.[15,21,27] Such complex engineering and processing steps limit 2DEG practical applications in functional electronic devices. Thus, current research on the 2DEG conductive heterointerface has mainly been limited to the study of its physical phenomena, but there has been no significant progress in the design and processing of electronic devices.

Recently, a simplified Al_2O_3 deposition process by atomic layered deposition (ALD) at low temperatures (<300 °C) was found to form the conductive 2DEG interface, overcoming the harsh preparation conditions of the LAO/STO system and providing a way to design and engineer this conductive heterointerface.[33−37] Among ALD of Al_2O_3 layers on single or polycrystalline metal oxide layers, several types of conductive heterointerfaces have been fabricated, including In_2O_3/Al_2O_3,[33,34] ZnO/Al_2O_3,[35] WO_3/Al_2O_3,[36] and TiO_2/Al_2O_3.[37,38] The two main factors responsible for the formation of conductive 2DEGs at the heterointerface are oxygen vacancies (V_o) at the interface and cation interdiffusion at the interface.[34,36−38] A representative study directly analyzed the chemical composition of the In_2O_3/Al_2O_3 interface by combining cross-sectional high-resolution transmission elec-

Received: March 13, 2023
Accepted: July 10, 2023
Published: July 24, 2023

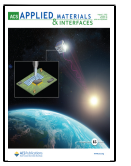

https://doi.org/10.1021/acsami.3c03603
ACS Appl. Mater. Interfaces 2023, 15, 36866−36876

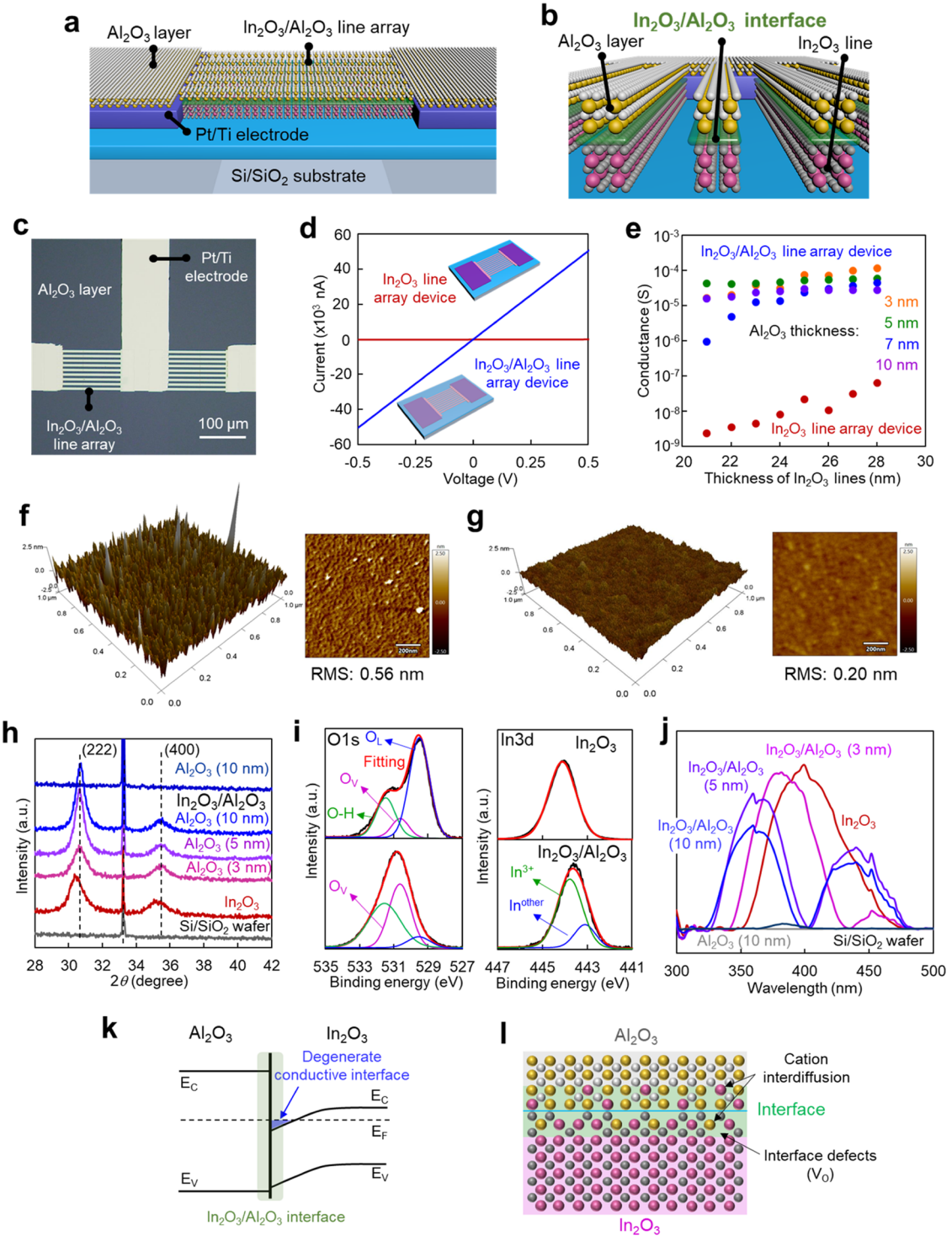

Figure 1. Fabrication of the degenerate 2DEG at the In_2O_3/Al_2O_3 heterointerface. (a) Schematic of the In_2O_3/Al_2O_3 line array device. (b) Schematic of the In_2O_3/Al_2O_3 interface. (c) Example microscopy image of the In_2O_3/Al_2O_3 line array device. The scale bar is 100 μm. (d) $I-V$ curves of In_2O_3 and In_2O_3/Al_2O_3 line array devices. (e) Conductance of In_2O_3 and In_2O_3/Al_2O_3 line array devices when varying the thicknesses of In_2O_3 and Al_2O_3. (f, g) Atomic force microscopy (AFM) images of the In_2O_3 and In_2O_3/Al_2O_3 layers. (h) X-ray diffraction (XRD) patterns of Al_2O_3, In_2O_3, and In_2O_3/Al_2O_3 layers with different Al_2O_3 thicknesses and Si/SiO_2 substrate. (i) XPS spectra of the In_2O_3 and In_2O_3/Al_2O_3 layers. (j) Photoluminescence (PL) spectra of In_2O_3, Al_2O_3, and In_2O_3/Al_2O_3 layers with different Al_2O_3 thicknesses and Si/SiO_2 substrate. (k) Estimated band alignment diagram of the In_2O_3/Al_2O_3 interface, which demonstrates the degenerate conductive interface. (l) Schematic of the In_2O_3/Al_2O_3 interface, which describes the interface defects and interdiffusion.

tron microscopy (HR-TEM), electron energy loss spectroscopy (EELS), and depth-resolved X-ray photoelectron spectroscopy (XPS) techniques and proposed a formation mechanism model for a 2DEG conducting path at the In_2O_3/Al_2O_3 interface.[34] However, the relationship between the chemical composition and electrical conductivity cannot be directly illustrated by an analysis of the chemical composition of an individual interface. No systematic and dynamic experimental

https://doi.org/10.1021/acsami.3c03603
ACS Appl. Mater. Interfaces 2023, 15, 36866−36876

study has been made to demonstrate the impact of key factors of interface defects and cation interdiffusion on the formation of this conductive interface. In addition, engineering this conductive 2DEG interface and exploring its applications in functional electronic devices have not yet been carried out.

In this work, based on current knowledge of the conductive 2DEG at the In_2O_3/Al_2O_3 interface, we conducted a systematic experimental study using oxygen plasma pretreatment and thermal annealing post-treatment to respectively engineer interface defects and cation interdiffusion at the In_2O_3/Al_2O_3 interface and further understanding of the formation mechanism of the conductive interface. By engineering different interfaces, we found that the interfacial defects facilitated the formation of the degenerate conductive interface, while cation interdiffusion at this interface degraded it. This implies that the thickening of the cation interdiffusion layer is detrimental to the formation of the conductive interface, which is different from past results. Considering the advantages of the conductive interface with a highly stable upper Al_2O_3 layer, this interface was processed as the electrodes in a field-effect transistor (FET) device and exhibited high stability in the PBS solution. This result represents the first realization of a 2DEG-based conductive interface electrode in an electronic device and shows potential for further applications in bioelectronic devices.

2. EXPERIMENTAL SECTION

2.1. Fabrication of an In_2O_3/Al_2O_3 Line Array Device and an FET Device. An In_2O_3/Al_2O_3 line array device (Figure 1a) was fabricated on a Si/SiO_2 (SiO_2 layer: 100 nm thick) substrate using the typical lithography method described in our previous reports.[39−42] In all our fabrications, the In_2O_3 layer was deposited by radio frequency (RF) sputtering and the deposition rate was about 5 nm/min (Figure S1a). We obtained 20−30 nm thick In_2O_3 lines by controlling the deposition time. The In_2O_3/Al_2O_3 line array was obtained by depositing an Al_2O_3 layer on the In_2O_3 lines using ALD. The Al source of trimethylaluminum (TMA) and O source of water were used to form a thin Al_2O_3 (3−10 nm) layer at 150 °C. The fluxes of TMA and water were controlled by the deposition times of 0.015 and 0.1 s, respectively.

A back-gated FET device with a line array channel was fabricated by adding a back-gated electrode on the In_2O_3/Al_2O_3 line array device. More specifically, a hole was made in the SiO_2 layer on the SiO_2/Si substrate at an edge position of the device to get direct contact between the Pt/Ti electrode and the Si layer below the SiO_2 layer.

2.2. Fabrication of an In_2O_3/Al_2O_3 Interface Electrode Device. An In_2O_3/Al_2O_3 interface electrode device was fabricated using In_2O_3/Al_2O_3 as the electrode and In_2O_3 as the channel. First, a large pattern with regions of both the line array and electrodes (Figure 1b) was prepared by the lithography technique. The patterned In_2O_3 layer was obtained by depositing In_2O_3 using RF sputtering. Then, a small pattern with the photoresist only at the position of the In_2O_3 line array was obtained using the second lithography step. Next, the Al_2O_3 layer was deposited in 40 cycles by ALD at 150 °C. The device was immersed in acetone to remove the photoresist above the line array. Last, IPA washing and N_2 flow drying were performed to get a clean device. In this case, a window in the Al_2O_3 layer at the In_2O_3 line array region was obtained. The In_2O_3/Al_2O_3 region acts as the electrode, while the In_2O_3 line array in the window region acts as the channel.

2.3. Characterizations. The structure of the In_2O_3/Al_2O_3 line array device was observed using optical microscopy images (Figure 1c). The crystalline phases of In_2O_3 and In_2O_3/Al_2O_3 layers were measured by X-ray diffraction (XRD, Rigaku Miniflex 600). The interdiffusion at the In_2O_3/Al_2O_3 interface was analyzed from the XRD pattern. The valence band and defects of In_2O_3 and In_2O_3/Al_2O_3 layers were characterized by photoluminescence (PL) spectra, which were measured using a fluorescent spectrophotometer (JASCO FP-8600) equipped with a xenon lamp as the excitation source. The excitation wavelength was set to 280 nm. The deposition rate of the In_2O_3 layer was characterized using a field-emission scanning electron microscope (FESEM, Zeiss Supra 40 VP) at an accelerating voltage of 15 kV. The surface profile was characterized by an atomic force microscope (AFM, MFP-3D Origin, Oxford Instruments). The chemical composition of the In_2O_3 and In_2O_3/Al_2O_3 layers was investigated by X-ray photoelectron spectroscopy (XPS, ULVAC-PHI VersaProbe III) with an Al Kα radiation ($h\gamma$ = 1486.6 eV). Raman spectra were conducted using a spectrometer (LabRAM HR800, HORIBA JobinYvon) with an excitation laser wavelength of 514.5 nm.

2.4. Electrical Measurements. The current−voltage ($I-V$) curve, transfer curve, and UV photoresponse (365 nm) were measured by two connected semiconductor parameter analyzers (Keithley, Model 2401). All of the measurements were done at room temperature.

3. RESULTS AND DISCUSSION

3.1. Formation of Degenerate 2DEG at the In_2O_3/Al_2O_3 Heterointerface. Figure 1a,b shows schematics of the In_2O_3/Al_2O_3 line array device and the In_2O_3/Al_2O_3 interface, respectively. An array of nine In_2O_3/Al_2O_3 lines with a width of 5 μm and a length of 120 μm served as the electron transport channel of the device (Figure 1c). The current−voltage ($I-V$) curves show that the In_2O_3/Al_2O_3 line array device possessed higher conductivity than the In_2O_3 line array device (Figure 1d). To evaluate the enhanced conductivity, the conductance of In_2O_3 and In_2O_3/Al_2O_3 line arrays of various line thicknesses was calculated based on the $I-V$ curves (Figure 1e). Compared to the In_2O_3 line array, the conductance of the In_2O_3/Al_2O_3 line array was approximately 4 orders of magnitude higher. As both the In_2O_3 line array and Al_2O_3 layer maintained low conductance during the ALD process (Figure S3), we confirmed that the enhanced conductance of the In_2O_3/Al_2O_3 line array originated from the In_2O_3/Al_2O_3 interface.

To understand the reason for the high electrical conductivity at the In_2O_3/Al_2O_3 interface, we analyzed the structure, chemical composition, and electrical transport behavior of the In_2O_3 and In_2O_3/Al_2O_3 layers. From the AFM images (Figure 1f,g), we observed that the surface of the film has been smoother after depositing the Al_2O_3 layer. As shown in XRD patterns, the diffraction peaks of the In_2O_3/Al_2O_3 layers were shifted toward a higher 2θ angle in comparison with the In_2O_3 layer (Figure 1h), while the diffraction peak of the Si substrate remained unshifted. This shift behavior could be attributed to the formation of a new phase of the intermixing layer at the In_2O_3/Al_2O_3 interface owing to the atom interdiffusion.[43−45] As shown in the XPS spectra of Figure 1i, two peaks attributed to the O 1s spectrum located between 527 and 535 eV were replaced by a broad peak at 439.9 eV. By fitting the spectrum based on three chemical binding states, including oxygen lattice (O_L), oxygen vacancy (O_V), and hydroxyl (−O−H),[34,46,47] we suggested that a large amount of O_V was generated close to the interface during its formation. We also made a simplified fitting of the In 3d spectrum using two binding states, the stable In state (In^{3+}), and the other In state (In^{other}).[34,46,47] The shift of the In 3d spectrum indicated a change in the In-related binding state, which was caused by the interactions of In, O, and Al atoms at the interface. In combination with the XRD results, we believe that this peak shift was caused by the interdiffusion of atoms at the interface.

https://doi.org/10.1021/acsami.3c03603
ACS Appl. Mater. Interfaces 2023, 15, 36866−36876

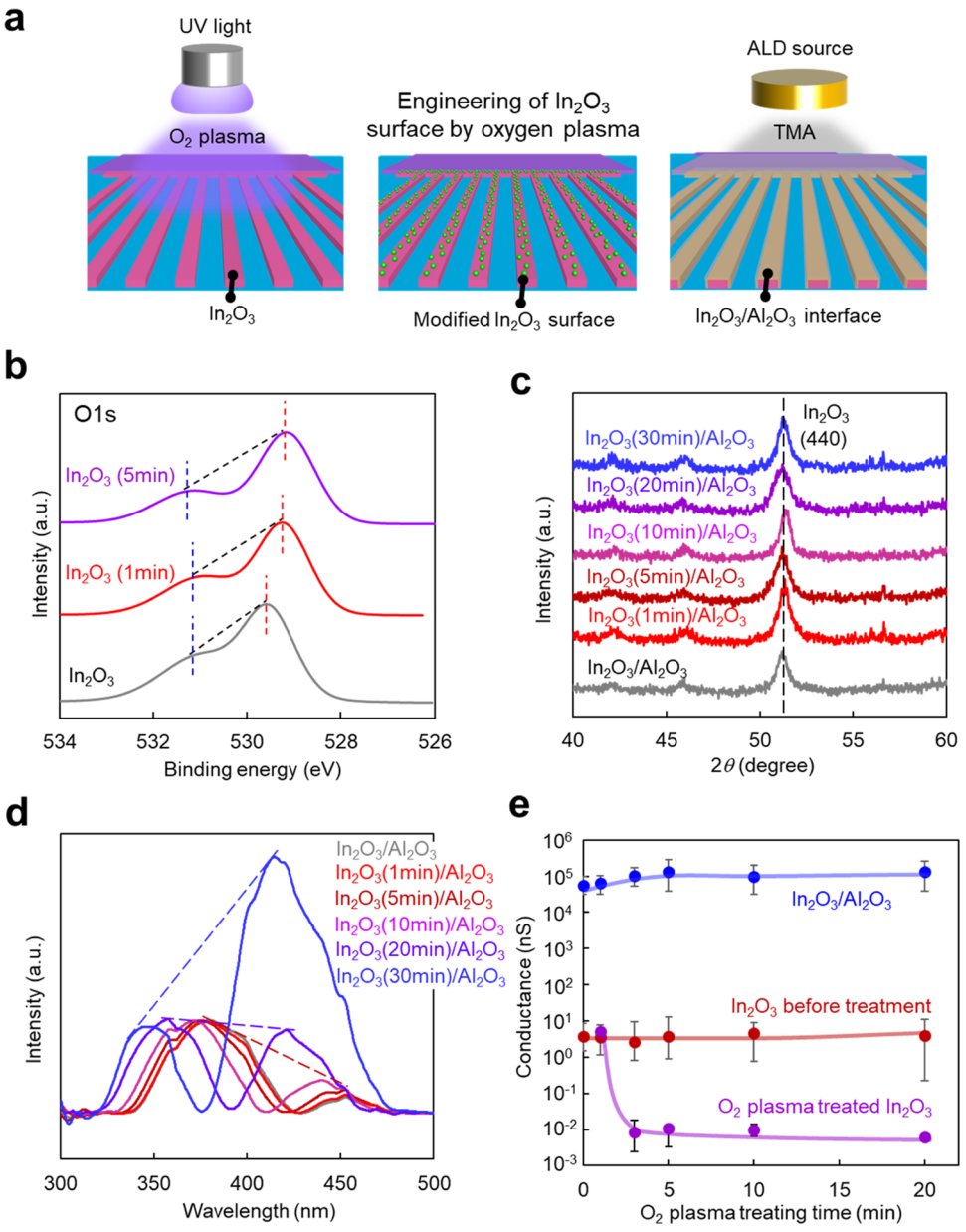

Figure 2. Engineering the interface defects of the In_2O_3/Al_2O_3 interface. (a) Schematics of pretreatment of the In_2O_3 surface prior to Al_2O_3 deposition. (b) XPS spectra of the In_2O_3 layer with different oxygen plasma pretreatment times. (c) XRD patterns of In_2O_3/Al_2O_3 layers with different oxygen plasma pretreatment times of the In_2O_3 surface. (d) PL spectra of In_2O_3/Al_2O_3 layers with different oxygen plasma pretreatment times of the In_2O_3 surface. (e) Conductance of In_2O_3 and In_2O_3/Al_2O_3 line arrays with different oxygen plasma pretreatment times of the In_2O_3 surface.

In addition, we found that on the In_2O_3 layer, the near-band-edge (NBE) emission peak shifted toward lower wavelengths from 402 to 361 nm after depositing the Al_2O_3 layer, which was consistent with a Burstein−Moss shift due to conduction band filling of the carriers (Figure 1j).[4] This suggested that high-concentration carriers were localized at the In_2O_3/Al_2O_3 interface that formed a metallic degenerate conductive interface, which can be described in terms of a 2DEG (Figure S4).[4,34,35,38]

Finally, transfer curves of the In_2O_3/Al_2O_3 line array, which was the "normally on" state, also indicated that the In_2O_3/Al_2O_3 interface exhibited a conductive property with a high carrier concentration, while In_2O_3 exhibited the typical semiconductor property (Figure S5).[48] Furthermore, UV photoresponse provided other indirect evidence of the conductive property of the In_2O_3/Al_2O_3 line array (Figure S6). While the In_2O_3 line array showed a current response to UV light of two orders of magnitude, the In_2O_3/Al_2O_3 line array maintained an almost constant current, even when the effect of high current compared to the In_2O_3 line array was eliminated by applying a low voltage of 0.001 V. This indicated that the enhancement of the current by UV-excited photoelectrons in the In_2O_3 line array was almost negligible compared to the high concentration of electrons at the In_2O_3/Al_2O_3 interface.[49] In addition, the flat subthreshold slope of the transfer curve and slow photoresponse observed from the electrical measurements indicated a low carrier mobility at the interface.[48,49] This result also demonstrated that the enhanced conductivity of the interface was caused by the high carrier concentration. All of the interpretations of the

https://doi.org/10.1021/acsami.3c03603
ACS Appl. Mater. Interfaces 2023, 15, 36866−36876

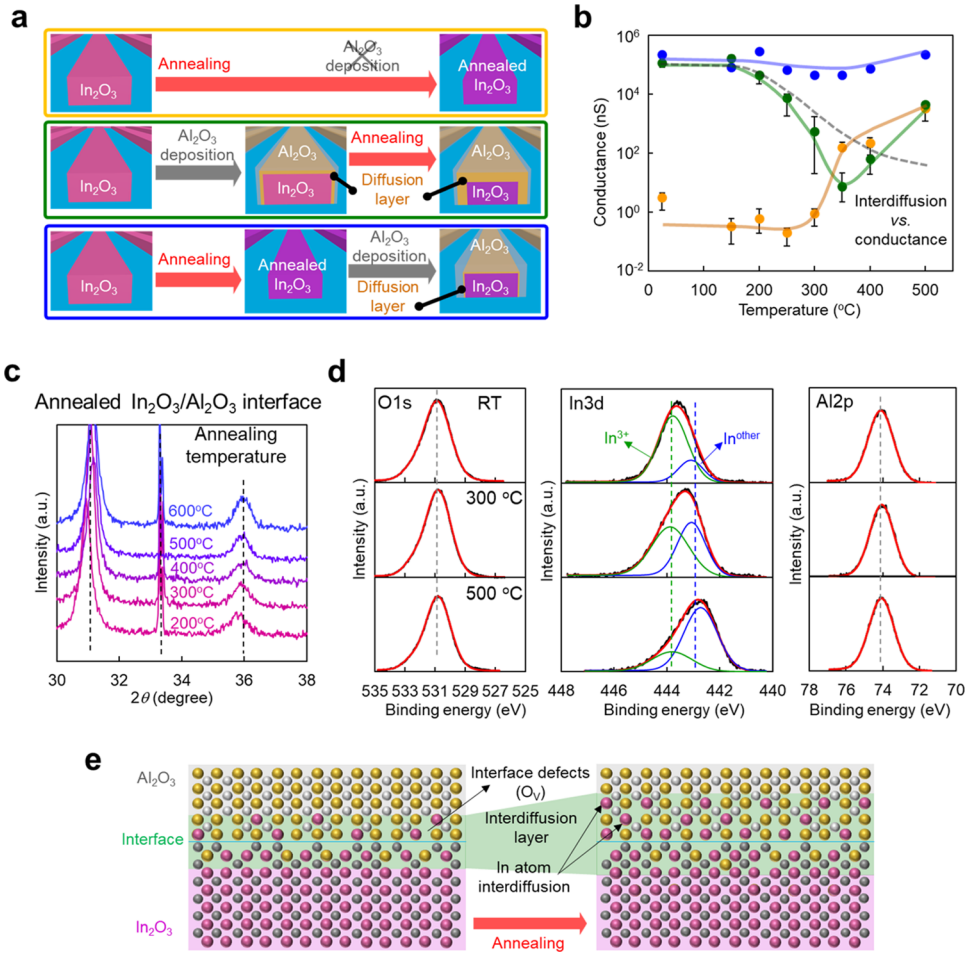

Figure 3. Engineering the interdiffusion of the Al_2O_3/In_2O_3 interface. (a) Schematic of three kinds of annealing processes of In_2O_3 and In_2O_3/Al_2O_3 line arrays. (1) Yellow box: In_2O_3 line arrays were annealed at different temperatures. (2) Blue box: first, In_2O_3 line arrays were annealed at different temperatures, followed by deposition of Al_2O_3 by ALD. (3) Green box: first, Al_2O_3 was deposited by ALD on the In_2O_3 line array, followed by annealing at different temperatures. (b) Annealing temperature-dependent conductance of In_2O_3 and In_2O_3/Al_2O_3 line arrays in three kinds of annealing processes. The annealing conditions for the different colored curves correspond to the colored boxes in Figure 4a. The gray dashed line shows the estimated curve of interdiffusion-dependent conductance. (c) XRD patterns of In_2O_3/Al_2O_3 layers annealed at different temperatures in air. (d) XPS spectra of In_2O_3/Al_2O_3 layers annealed at different temperatures in air. (e) Schematic of the model for the interdiffusion-dependent conductive In_2O_3 and Al_2O_3 interface.

above data suggested that this conductive In_2O_3/Al_2O_3 interface was a degenerate 2DEG with a high carrier concentration, which was described by the band diagram of Figure 1k.[50−52]

Currently, the three most accepted scenarios to describe the mechanism of 2DEG formation using amorphous Al_2O_3 are a polar catastrophe, cation interdiffusion, and oxygen vacancy (V_o) generation at the interface.[34,38] Based on the analysis of structure, composition, and electrical transport behavior of the In_2O_3/Al_2O_3 layer, we suggested that the interface defects (V_o) and cation interdiffusion at the interface were crucial factors in the formation of such a conductive In_2O_3/Al_2O_3 interface. However, the relationship between the structure, chemical composition, and electrical conductivity cannot be easily demonstrated by analysis of an individual interface. Therefore, to further understand this conductive In_2O_3/Al_2O_3 interface, we undertook systematic experiments, in which we engineered interface defects and cation interdiffusion at the interface, as depicted in the schematic of Figure 1l. In addition, by engineering the above factors, we were seeking an approach to control this conductive interface, for example, to get a more stable fabrication method, to gain a higher conductivity enhancement, etc.

3.2. Engineering Interface Defects of the In_2O_3/Al_2O_3 Heterointerface. First, we considered the formation and engineering of interface defects at the In_2O_3/Al_2O_3 interface using an In_2O_3 surface pretreated by oxygen plasma before Al_2O_3 deposition (Figure 2a). This is because the oxygen plasma treatment generally enhances the number of hydrophilic groups on metal oxide surfaces, especially for hydroxyl groups,[53] which may affect the generation of interface defects at the In_2O_3/Al_2O_3 interface during ALD. As seen in the XPS spectra (Figure 2b), the O 1s peak located at 529.6 eV shifted toward a lower energy direction after the oxygen plasma pretreatment in In_2O_3 layers, suggesting that the binding state changed from the O_V state to the O_L state. This is caused by the oxidization of oxygen-deficient In_2O_3 during the oxygen plasma treatment.[54] A slight shift of the peak located at 531.2 eV indicated an increase of the O−H bonding on the surface. In other words, the hydroxyl groups on the surface were increased by oxygen plasma treatment. The crystalline phase of In_2O_3 was confirmed by the XRD pattern, and no peak shift

https://doi.org/10.1021/acsami.3c03603
ACS Appl. Mater. Interfaces 2023, 15, 36866−36876

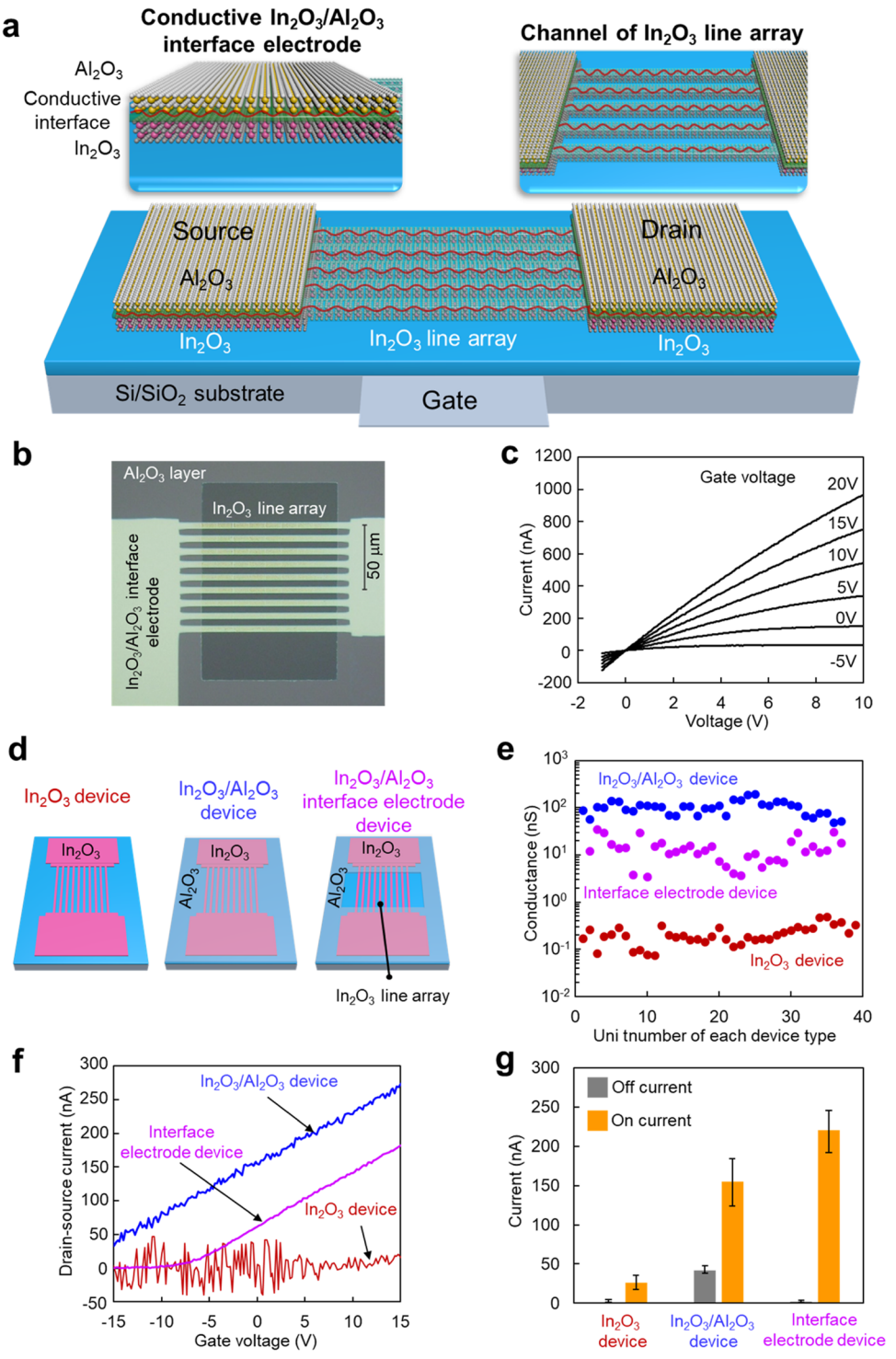

Figure 4. Processing the conductive In_2O_3/Al_2O_3 interface as the interface electrode. (a) Schematic of the FET device with the In_2O_3 line array as the electron transport channel and the In_2O_3/Al_2O_3 conductive interface as the interface electrode. (b) Microscopy image of the device. A window was opened at the In_2O_3 line array region to fabricate the device. (c) Representative output curves of the device with gate voltage as a function. The drain−source voltage was 1 V. (d) Schematic of three kinds of devices. (1) The In_2O_3 device is patterned In_2O_3 with the In_2O_3 line array as the transport channel and In_2O_3 as the electrode. (2) The In_2O_3/Al_2O_3 device is patterned In_2O_3/Al_2O_3 with the In_2O_3/Al_2O_3 line array as the transport channel and In_2O_3/Al_2O_3 as the electrode. (3) The In_2O_3/Al_2O_3 interface electrode device is patterned In_2O_3 with the In_2O_3 line array as the transport channel and the In_2O_3/Al_2O_3 as the electrode. (e) Measured conductance of the In_2O_3 device, In_2O_3/Al_2O_3 device, and In_2O_3/Al_2O_3 interface electrode device. (f) Transfer curves of the In_2O_3 device, In_2O_3/Al_2O_3 device, and In_2O_3/Al_2O_3 interface electrode device. The drain−source voltage is 1 V. (g) Comparison of "on" current (applied gate voltage: 10 V) and "off" current (applied gate voltage: −10 V) of the In_2O_3 device, In_2O_3/Al_2O_3 device, and In_2O_3/Al_2O_3 interface electrode device.

was observed (Figure 2c). In contrast to the XRD results in Figure 1h, which indicated that the shift of the peaks was caused by interdiffusion, interdiffusion at the interface was not changed by the oxygen plasma pretreatment. When oxygen

https://doi.org/10.1021/acsami.3c03603
ACS Appl. Mater. Interfaces 2023, 15, 36866−36876

plasma treatment time was increased, a blue shift in the NBE peak of the pretreated In_2O_3/Al_2O_3 layers (implying degenerate character) was observed and the peak ratio of the defect and NBE peaks increased, as shown in the PL spectra of Figure 2d. This means that the degenerate interface with additional defects might also be formed when the oxygen plasma pretreatment was applied.[4]

In addition, the conductance of In_2O_3 line arrays decreased with increasing oxygen plasma treatment time, while the conductance of In_2O_3/Al_2O_3 line arrays increased slightly (Figure 2e). Based on the analysis of the above characterization, we believe that two factors contributed to the reduction of the conductivity of the In_2O_3 layer by oxygen plasma treatment: (1) reducing the conductive oxygen vacancies in the metal oxide[54] and (2) increasing the number of surface hydroxyl groups that trap carriers. Since the conductance of the oxygen plasma pretreated In_2O_3/Al_2O_3 interface always increased after Al_2O_3 deposition, we speculated that the oxygen vacancies were refilled during the ALD process or the oxygen vacancies within the In_2O_3 body produced a tiny effect on interface conductance.[54] This is because the reduction of the oxygen vacancies generally reduces the electrical conductivity. Therefore, we have ignored the effect of oxygen vacancy fluctuations and focused on the effect of the increased numbers of hydroxyl groups on the In_2O_3 surface. In this case, the conductance of the In_2O_3/Al_2O_3 line array increased with increasing pretreatment time, which could be attributed to the increase in shallow-level interface defects (e.g., oxygen vacancies), as the interdiffusion remained unchanged during the process. This means the hydroxyl groups on the In_2O_3 surface might facilitate the generation of shallow-level interface defects during the ALD of the Al_2O_3 layer. Although the formation mechanism of these shallow-level interface defects was not clear, we can conclude that the groups generated on the In_2O_3 surface by the oxygen plasma treatment will promote the generation of conductive interface defects, leading to increased conductance of the In_2O_3/Al_2O_3 interface. Therefore, the interface defects that facilitate the formation of such degenerate conductive interfaces can be engineered by oxygen plasma pretreatment, and these defects can further increase the conductivity of the In_2O_3/Al_2O_3 interface.

3.3. Engineering Interdiffusion of the Al_2O_3/In_2O_3 Heterointerface. Next, we considered if interdiffusion occurred at the In_2O_3/Al_2O_3 interface during the ALD of the Al_2O_3 layer and if it could be engineered by a postannealing process, as thermal annealing always facilitates atom diffusion.[55−57] The effect of interdiffusion at the In_2O_3/Al_2O_3 interface on the electrical conductance was investigated by altering the sequence of Al_2O_3 deposition and thermal annealing treatment. Three kinds of annealing processes were conducted as summarized in Figure 3a. Diffraction peaks of XRD patterns were gradually shifted toward the higher angle direction by increasing the annealing temperature from 200 to 600 °C (Figure 3c), indicating that the interdiffusion at the interface can be controlled by the annealing process.

Temperature-dependent conductance showed that the conductance of the In_2O_3 line array increased with annealing temperature from 250 to 500 °C, which is generally due to the generation of shallow-level defects, such as oxygen vacancies or indium interstitial defects.[58,59] When directly annealing the In_2O_3/Al_2O_3 line array, the conductance decreased first and increased above 350 °C. To clarify the trend of this variation, we measured the XPS spectra of In_2O_3/Al_2O_3 layers annealed at 300 and 500 °C, as shown in Figure 3d. The In 3d peak shifted toward lower energies with increasing annealing temperature, while the O 1s and Al 2p peaks remained at 539.9 and 74.2 eV, respectively.[60,61] This indicated that the change in the In binding state played a dominant role compared to the change in the oxygen and Al binding states. Based on the fitting results of the In 3d peak, in which the binding state of In^{3+} was converted to In^{other}, we speculated that the interdiffusion of In at the interface was the main behavior and led to a decrease in conductance, as shown in the schematic of Figure 3e. The conductance increased above 350 °C was due to the increased conductance of the In_2O_3 line array.

In addition, when Al_2O_3 was deposited by ALD after annealing the In_2O_3 line array, the In_2O_3 line array with enhanced crystallization would prevent the interdiffusion of Al_2O_3 during the ALD. The conductance of the In_2O_3/Al_2O_3 line array remained consistently high and increased slightly above 300 °C, which agreed with the enhanced conductance of annealed In_2O_3 line arrays. The above results indicated that the interdiffusion at the In_2O_3/Al_2O_3 interface was detrimental to the formation of the degenerate conductive 2DEG, which differs from the previous understanding.[34] In other words, preannealing of the In_2O_3 layer prior to deposition of Al_2O_3 by ALD suppressed interdiffusion at the interface and was beneficial to the formation of the degenerate conductive interface. Thus, based on the results of the engineering experiments, we concluded that the formation of the degenerate interface was mainly due to the generation of interface defects (V_O) rather than the In cation interdiffusion at the interface. Since the conductance of this interface was always kept at a high value when In interdiffusion was suppressed by preannealing of the In_2O_3 layer, we believe that the interface defects were confined in an ultrathin interdiffusion layer of the interface. When interdiffusion at the interface was facilitated by the annealing, the enhanced interdiffusion layer upset the equilibrium of interface defects in the ultrathin layer at the interface. This means that building a sharp interface with a high concentration of shallow interface defects is beneficial to obtain such a conductive degenerate interface. Experimentally, we found that pretreatments of annealing and oxygen plasma on the In_2O_3 layer provided a more stable fabrication method for preparing this conductive interface.

3.4. Processing the Conductive In_2O_3/Al_2O_3 Interface as a Stable Interface Electrode in Saline Solution. Finally, we demonstrated an example application of this degenerate interface in a functional electronic device, that is, the fabrication of an In_2O_3 line array FET device with the In_2O_3/Al_2O_3 interface electrode (Figure 4a). As shown in Figure 4b, the semiconducting In_2O_3 line array in the window served as the electron transport channel, while the other regions with the conductive In_2O_3/Al_2O_3 interface served as the electrodes. Representative output characteristics of the FET device with interface electrodes at various gate voltages from −5 to 20 V indicated that our degenerate In_2O_3/Al_2O_3 interface was being used as the interface electrode for the FET device (Figure 4c). Compared to the In_2O_3 and In_2O_3/Al_2O_3 devices (Figure 4d), the In_2O_3/Al_2O_3 interface electrode device showed conductance values between the other devices (Figure 4e), which was consistent with our conductance results above. The transfer curves of the three kinds of FET devices showed that only the In_2O_3/Al_2O_3 interface electrode device

https://doi.org/10.1021/acsami.3c03603
ACS Appl. Mater. Interfaces 2023, 15, 36866−36876

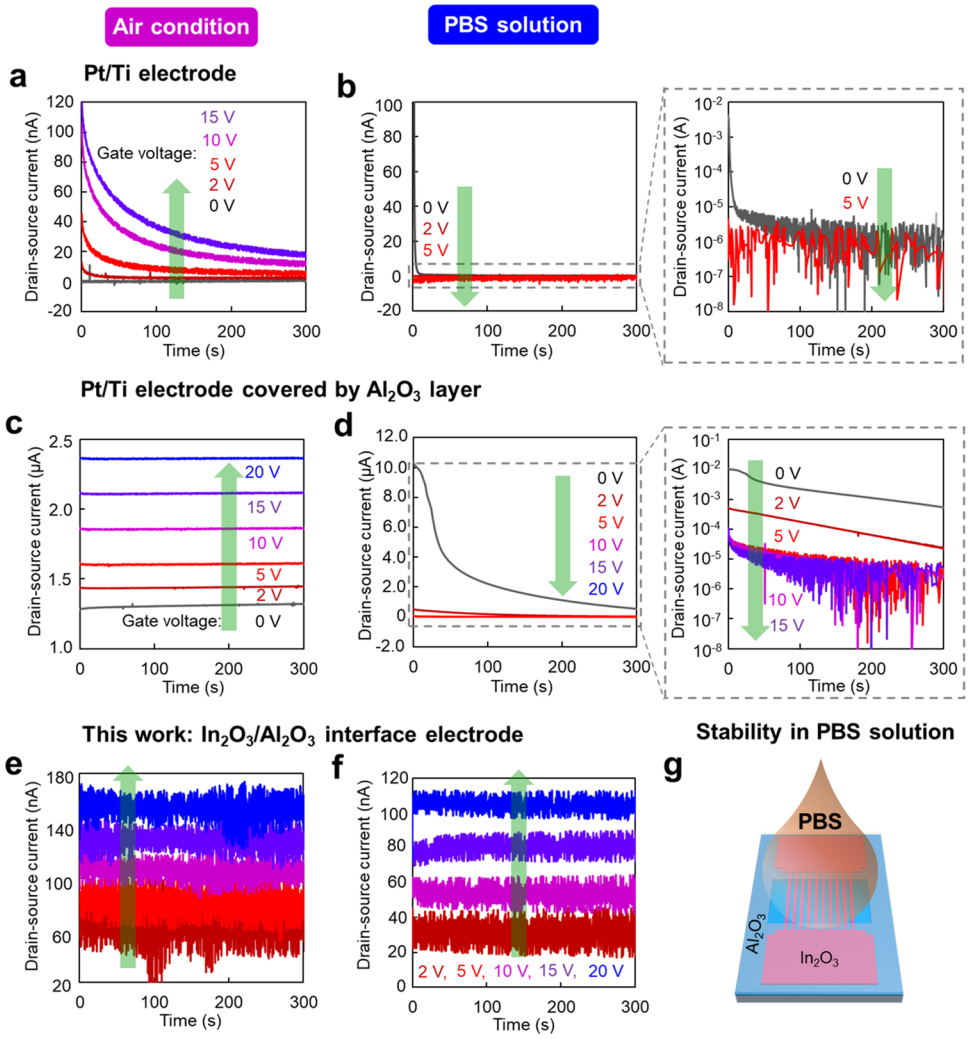

Figure 5. Stability of the In_2O_3/Al_2O_3 interface electrode in the PBS solution. (a, b) Stability of the In_2O_3 FET device with Pt/Ti as an electrode in (a) air condition and (b) PBS solution when varying gate voltage. (c, d) Stability of the device with the Pt/Ti electrode after covering an Al_2O_3 layer in (c) air condition and (d) PBS solution. (e, f) Stability of the device with the In_2O_3/Al_2O_3 interface electrode in (e) air condition and (f) PBS solution. (g) Schematic of stability testing in the PBS solution of the device with the In_2O_3/Al_2O_3 interface electrode. The exponential coordinate of the current was shown in the right section of panels (b) and (d). The gate voltage of all devices was respectively set to 0, 2, 5, 10, and 15 V during the stability test. The thickness of the Al_2O_3 layer on the Pt/Ti electrode was set to 5 nm, which is the same as the In_2O_3/Al_2O_3 interface electrode.

exhibited the typical depletion and enhancement modes of current modulation when an electric field was introduced (Figure 4f). In contrast, the In_2O_3/Al_2O_3 device always exhibited high conductance, while the In_2O_3 device exhibited low conductance, even when an electric field was applied. To clearly show the modulation effect, the "on" current and "off" current were extracted (Figure 4g), and the highest ratio of "on" current to "off" current for the In_2O_3/Al_2O_3 interface electrode FET device indicated that this FET device had the optimal modulation capability to control the conductance.

Since this interface has an upper Al_2O_3 layer that is stable to body fluids, we tested the stability of this device in a saline solution (PBS), which is shown in Figure 5. To evaluate the stability of such an interface electrode in an FET device, the devices with the Pt/Ti electrode and the Pt/Ti electrode covered by an Al_2O_3 layer were also fabricated for comparison of performance. In air conditions, all of the devices showed increased current when increasing the gate voltage (Figure 5a,c,e). The devices with the Pt/Ti electrode covered by an Al_2O_3 layer and In_2O_3/Al_2O_3 interface electrode showed a very stable current with increasing test time compared to the device with the Pt/Ti electrode, which is due to the protective effect of the Al_2O_3 layer against the molecules in the air. When tested in the PBS solution, the current of the device with the Pt/Ti electrode dropped abruptly, and it still decreased with increasing gate voltage despite being covered by an Al_2O_3 layer (Figure 5b,d). In contrast, the device with our interface electrode exhibited an increase in current with increasing gate voltage, as well as the current, remained stable with increasing time, indicating the high stability of the interface electrode in the PBS solution (Figure 5f). Our results prove that the degenerate In_2O_3/Al_2O_3 interface electrode exhibited high stability in biological saline and showed its potential for applications in functional bioelectronics.

4. CONCLUSIONS

We carried out systematic experiments of oxygen plasma pretreatment and thermal annealing post-treatment to study

https://doi.org/10.1021/acsami.3c03603
ACS Appl. Mater. Interfaces 2023, 15, 36866−36876

the engineering of interface defects and In interdiffusion at the degenerate conductive Al_2O_3/In_2O_3 interface. Interface defects engineered by using oxygen plasma pretreatment on the In_2O_3 surface prior to Al_2O_3 deposition indicated that shallow interface defects facilitated the formation of conductive interfaces. Interdiffusion at the In_2O_3/Al_2O_3 interface engineered by thermal annealing seemed to degrade the degenerate conductive interface. While past studies have suggested that a semimetallic intermixing layer at the interface promotes the formation of a 2DEG at the In_2O_3/Al_2O_3 interface, we demonstrated a negative effect of interface diffusion on the conductive interface. Based on these findings, we found that pretreatments of annealing and oxygen plasma on the In_2O_3 layer provided a more stable fabrication method for preparing this conductive interface. After applying this conductive interface as an interface electrode for an FET device, we found that this interface electrode exhibited ultrastability in a biological saline solution. This work lays the foundation for controlling a highly conductive degenerate 2DEG at metal oxide/Al_2O_3 interfaces and exploring its potential applications in functional bioelectronic devices.

■ ASSOCIATED CONTENT

Supporting Information

The Supporting Information is available free of charge at https://pubs.acs.org/doi/10.1021/acsami.3c03603.

SEM images (Figure S1); Raman spectra (Figure S2); conductance (Figure S3); band structure (Figure S4); transfer curves (Figure S5); UV response curves of In_2O_3 and In_2O_3/Al_2O_3 (Figure S6); conductance of the annealed interface (Figure S7); and microscopy images of devices (Figure S8) (PDF)

■ AUTHOR INFORMATION

Corresponding Authors

Zetao Zhu − *Department of Biomolecular Engineering, Graduate School of Engineering, Nagoya University, Nagoya 464-8603, Japan; Institute of Nano-Life-Systems, Institutes of Innovation for Future Society, Nagoya University, Nagoya 464-8603, Japan;* orcid.org/0000-0001-6156-748X; Phone: +81-52-789-3560; Email: zhuzetao@nanobio.nagoya-u.ac.jp

Takao Yasui − *Department of Biomolecular Engineering, Graduate School of Engineering, Nagoya University, Nagoya 464-8603, Japan; Institute of Nano-Life-Systems, Institutes of Innovation for Future Society, Nagoya University, Nagoya 464-8603, Japan; Department of Life Science and Technology, Tokyo Institute of Technology, Yokohama 226-8501, Japan; Japan Science and Technology Agency (JST), Precursory Research for Embryonic Science and Technology (PRESTO), Kawaguchi 332-0012 Saitama, Japan;* orcid.org/0000-0003-0333-3559; Phone: +81-45-924-5520; Email: yasuit@bio.titech.ac.jp

Yoshinobu Baba − *Department of Biomolecular Engineering, Graduate School of Engineering, Nagoya University, Nagoya 464-8603, Japan; Institute of Nano-Life-Systems, Institutes of Innovation for Future Society, Nagoya University, Nagoya 464-8603, Japan; Institute of Quantum Life Science, National Institutes for Quantum Science and Technology (QST), Chiba 263-8555, Japan*; Phone: +81-52-789-4664; Email: babaymtt@chembio.nagoya-u.ac.jp

Authors

Xixi Zhao − *Department of Applied Chemistry, Graduate School of Engineering, The University of Tokyo, Tokyo 113-8656, Japan*

Quanli Liu − *Department of Biomolecular Engineering, Graduate School of Engineering, Nagoya University, Nagoya 464-8603, Japan*

Shu Morita − *Department of Materials Chemistry & Institute of Materials and Systems for Sustainability (IMaSS), Nagoya University, Nagoya 464-8603, Japan*

Yan Li − *Department of Materials Chemistry & Institute of Materials and Systems for Sustainability (IMaSS), Nagoya University, Nagoya 464-8603, Japan*

Akira Yonezu − *Department of Materials Chemistry, Graduate School of Engineering, Nagoya University, Nagoya 464-8603, Japan*

Kazuki Nagashima − *Japan Science and Technology Agency (JST), Precursory Research for Embryonic Science and Technology (PRESTO), Kawaguchi 332-0012 Saitama, Japan; Department of Applied Chemistry, Graduate School of Engineering, The University of Tokyo, Tokyo 113-8656, Japan;* orcid.org/0000-0003-0180-816X

Tsunaki Takahashi − *Japan Science and Technology Agency (JST), Precursory Research for Embryonic Science and Technology (PRESTO), Kawaguchi 332-0012 Saitama, Japan; Department of Applied Chemistry, Graduate School of Engineering, The University of Tokyo, Tokyo 113-8656, Japan;* orcid.org/0000-0002-2840-8038

Minoru Osada − *Department of Materials Chemistry & Institute of Materials and Systems for Sustainability (IMaSS), Nagoya University, Nagoya 464-8603, Japan;* orcid.org/0000-0002-6439-8068

Ryotaro Matsuda − *Department of Materials Chemistry, Graduate School of Engineering, Nagoya University, Nagoya 464-8603, Japan*

Takeshi Yanagida − *Department of Applied Chemistry, Graduate School of Engineering, The University of Tokyo, Tokyo 113-8656, Japan; Institute for Materials Chemistry and Engineering, Kyushu University, Kasuga 816-8580 Fukuoka, Japan;* orcid.org/0000-0003-4837-5701

Complete contact information is available at: https://pubs.acs.org/10.1021/acsami.3c03603

Author Contributions

Z.Z., T. Yasui, K.N., T.T., and T. Yanagida conceived and designed the overall research plan, experiments, and data analysis. Z.Z., T. Yasui, X.Z., Q.L., S.M., Y.L., A.Y., K.N., T.T., and M.O. developed the setups and performed experiments. X.Z. performed PL spectrum measurements. S.M. and Y.L. performed Raman, AFM, and XPS measurements. A.Y. provided support for the XRD measurement experiments. T. Yasui, T. Yanagida, and Y.B. contributed to conceptualization, funding acquisition, project administration, and supervision. Z.Z. and T. Yasui wrote the manuscript with the input of the other authors.

Notes

The authors declare no competing financial interest.

■ ACKNOWLEDGMENTS

This research was supported by the Japan Science and Technology Agency (JST) PRESTO (JPMJPR19H9), the JST SICORP (JPMJSC19E3), the New Energy and Industrial

Technology Development Organization (NEDO) JPNP20004, the Japan Agency for Medical Research and Development (AMED Grant Nos. JP21he2302007, 22zf0127004s0902, and 22zf0127009h0001), the JSPS Grant-in-Aid for Scientific Research (B) 21H01960, JST AIP Acceleration Research JPMJCR23U1, and the Cooperative Research Program of the "Network Joint Research Center for Materials and Devices". They also thank Dr. A. Arima for his valuable discussions.

REFERENCES

(1) Ohtomo, A.; Hwang, H. Y. A High-Mobility Electron Gas at the $LaAlO_3/SrTiO_3$ Heterointerface. *Nature* **2004**, *427*, 423−426.
(2) Reyren, N.; Thiel, S.; Caviglia, A. D.; Kourkoutis, L. F.; Hammerl, G.; Richter, C.; Schneider, C. W.; Kopp, T.; Rüetschi, A. S.; Jaccard, D.; Gabay, M.; Muller, D. A.; Triscone, J. M.; Mannhart, J. Superconducting Interfaces Between Insulating Oxides. *Science* **2007**, *317*, 1196−1199.
(3) Thiel, S.; Hammerl, G.; Schmehl, A.; Schneider, C. W.; Mannhart, J. Tunable Quasi-Two-Dimensional Electron Gases in Oxide Heterostructures. *Science* **2006**, *313*, 1942−1945.
(4) Ohta, H.; Kim, S.; Mune, Y.; Mizoguchi, T.; Nomura, K.; Ohta, S.; Nomura, T.; Nakanishi, Y.; Ikuhara, Y.; Hirano, M.; Hosono, H.; Koumoto, K. Giant Thermoelectric Seebeck Coefficient of a Two-Dimensional Electron Gas in $SrTiO_3$. *Nat. Mater.* **2007**, *6*, 129−134.
(5) Bandurin, D. A.; Tyurnina, Av.; Yu, G. L.; Mishchenko, A.; Zólyomi, V.; Morozov, Sv.; Kumar, R. K.; Gorbachev, Rv.; Kudrynskyi, Z. R.; Pezzini, S.; Kovalyuk, Z. D.; Zeitler, U.; Novoselov, K. S.; Patanè, A.; Eaves, L.; Grigorieva, Iv.; Fal'ko, V. I.; Geim, A. K.; Cao, Y. High Electron Mobility, Quantum Hall Effect and Anomalous Optical Response in Atomically Thin InSe. *Nat. Nanotechnol.* **2017**, *12*, 223−227.
(6) Han, Y. L.; Shen, S. C.; You, J.; Li, H. O.; Luo, Z. Z.; Li, C. J.; Qu, G. L.; Xiong, C. M.; Dou, R. F.; He, L.; Naugle, D.; Guo, G. P.; Nie, J. C. Two-Dimensional Superconductivity at (110) $LaAlO_3/SrTiO_3$ Interfaces. *Appl. Phys. Lett.* **2014**, *105*, No. 192603.
(7) Kalaboukhov, A.; Aurino, P. P.; Galletti, L.; Bauch, T.; Lombardi, F.; Winkler, D.; Claeson, T.; Golubev, D. Homogeneous Superconductivity at the $LaAlO_3/SrTiO_3$ Interface Probed by Nanoscale Transport. *Phys. Rev. B* **2017**, *96*, No. 184525.
(8) Strocov, V. N.; Chikina, A.; Caputo, M.; Husanu, M. A.; Bisti, F.; Bracher, D.; Schmitt, T.; Miletto Granozio, F.; Vaz, C. A. F.; Lechermann, F. Electronic Phase Separation at $LaAlO_3/SrTiO_3$ Interfaces Tunable by Oxygen Deficiency. *Phys. Rev. Mater.* **2019**, *3*, No. 106001.
(9) Bi, F.; Huang, M.; Lee, H.; Eom, C. B.; Irvin, P.; Levy, J. $LaAlO_3$ Thickness Window for Electronically Controlled Magnetism at $LaAlO_3/SrTiO_3$ Heterointerfaces. *Appl. Phys. Lett.* **2015**, *107*, No. 082402.
(10) Banerjee, S.; Erten, O.; Randeria, M. Ferromagnetic Exchange, Spin−Orbit Coupling and Spiral Magnetism at the $LaAlO_3/SrTiO_3$ Interface. *Nat. Phys.* **2013**, *9*, 626−630.
(11) Hu, H.-L.; Zeng, R.; Pham, A.; Tan, T. T.; Chen, Z.; Kong, C.; Wang, D.; Li, S. Subtle Interplay between Localized Magnetic Moments and Itinerant Electrons in $LaAlO_3/SrTiO_3$ Heterostructures. *ACS Appl. Mater. Interfaces* **2016**, *8*, 13630−13636.
(12) Aliaj, I.; Sambri, A.; Miseikis, V.; Stornaiuolo, D.; Gennaro, E.; Coletti, C.; Pellegrini, V.; Miletto Granozio, F.; Roddaro, S. Probing Charge Transfer during Metal-Insulator Transitions in Graphene-$LaAlO_3/SrTiO_3$ Systems. *APL Mater.* **2018**, *6*, No. 066103.
(13) Briggeman, M.; Tomczyk, M.; Tian, B.; Lee, H.; Lee, J. W.; He, Y.; Tylan-Tyler, A.; Huang, M.; Eom, C. B.; Pekker, D.; Mong, R. S. K.; Irvin, P.; Levy, J. Pascal Conductance Series in Ballistic One-Dimensional $LaAlO_3/SrTiO_3$ Channels. *Science* **2020**, *367*, 769−772.
(14) Trier, F.; Prawiroatmodjo, G. E. D. K.; Zhong, Z.; Christensen, D. V.; Soosten, M.; Bhowmik, A.; Lastra, J. M. G.; Chen, Y.; Jespersen, T. S.; Pryds, N. Quantization of Hall Resistance at the Metallic Interface between an Oxide Insulator and $SrTiO_3$. *Phys. Rev. Lett.* **2016**, *117*, No. 096804.
(15) Kornblum, L. Conductive Oxide Interfaces for Field Effect Devices. *Adv. Mater. Interfaces* **2019**, *6*, No. 1900480.
(16) Sharma, P.; Ryu, S.; Burton, J. D.; Paudel, T. R.; Bark, C. W.; Huang, Z.; Ariando; Tsymbal, E. Y.; Catalan, G.; Eom, C. B.; Gruverman, A. Mechanical Tuning of $LaAlO_3/SrTiO_3$ Interface Conductivity. *Nano Lett.* **2015**, *15*, 3547−3551.
(17) Woltmann, C.; Harada, T.; Boschker, H.; Srot, V.; van Aken, P. A.; Klauk, H.; Mannhart, J. Field-Effect Transistors with Submicrometer Gate Lengths Fabricated from $LaAlO_3$−$SrTiO_3$-Based Heterostructures. *Phys. Rev. Appl.* **2015**, *4*, No. 064003.
(18) Park, J. W.; Bogorin, D. F.; Cen, C.; Felker, D. A.; Zhang, Y.; Nelson, C. T.; Bark, C. W.; Folkman, C. M.; Pan, X. Q.; Rzchowski, M. S.; Levy, J.; Eom, C. B. Creation of a Two-Dimensional Electron Gas at an Oxide Interface on Silicon. *Nat. Commun.* **2010**, *1*, No. 94.
(19) Podkaminer, J. P.; Hernandez, T.; Huang, M.; Ryu, S.; Bark, C. W.; Baek, S. H.; Frederick, J. C.; Kim, T. H.; Cho, K. H.; Levy, J.; Rzchowski, M. S.; Eom, C. B. Creation of a Two-Dimensional Electron Gas and Conductivity Switching of Nanowires at the $LaAlO_3/SrTiO_3$ Interface Grown by 90° off-Axis Sputtering. *Appl. Phys. Lett.* **2013**, *103*, No. 071604.
(20) Ji, F.; Sharma, P.; Xin, T.; Zhang, D.; Liu, Y.; Niu, R.; Cairney, J. M.; Seidel, J. Lateral Gating of 2D Electron Gas in Cross-Sectional $LaAlO_3/SrTiO_3$. *Adv. Electron. Mater.* **2020**, *6*, No. 2000068.
(21) Yao, X.; Klyukin, K.; Lu, W.; Onen, M.; Ryu, S.; Kim, D.; Emond, N.; Waluyo, I.; Hunt, A.; del Alamo, J. A.; Li, J.; Yildiz, B. Protonic Solid-State Electrochemical Synapse for Physical Neural Networks. *Nat. Commun.* **2020**, *11*, No. 3134.
(22) Şahin, Z.; Meunier-Prest, R.; Dumoulin, F.; Kumar, A.; Isci, Ü.; Bouvet, M. Tuning of Organic Heterojunction Conductivity by the Substituents' Electronic Effects in Phthalocyanines for Ambipolar Gas Sensors. *Sens. Actuators, B* **2021**, *332*, No. 129505.
(23) Singh, T.; Öz, S.; Sasinska, A.; Frohnhoven, R.; Mathur, S.; Miyasaka, T. Sulfate-Assisted Interfacial Engineering for High Yield and Efficiency of Triple Cation Perovskite Solar Cells with Alkali-Doped TiO_2 Electron-Transporting Layers. *Adv. Funct. Mater.* **2018**, *28*, No. 1706287.
(24) Yang, K.; Xiao, J.; Ren, Z.; Wei, Z.; Luo, J. W.; Wei, S. H.; Deng, H. X. Decoupling of the Electrical and Thermal Transports in Strongly Coupled Interlayer Materials. *J. Phys. Chem. Lett.* **2021**, *12*, 7832−7839.
(25) Panzer, M. J.; Frisbie, C. D. Exploiting Ionic Coupling in Electronic Devices: Electrolyte-Gated Organic Field-Effect Transistors. *Adv. Mater.* **2008**, *20*, 3177−3180.
(26) Chen, Y. Z.; Bovet, N.; Trier, F.; Christensen, D. V.; Qu, F. M.; Andersen, N. H.; Kasama, T.; Zhang, W.; Giraud, R.; Dufouleur, J.; Jespersen, T. S.; Sun, J. R.; Smith, A.; Nygård, J.; Lu, L.; Büchner, B.; Shen, B. G.; Linderoth, S.; Pryds, N. A High-Mobility Two-Dimensional Electron Gas at the Spinel/Perovskite Interface of γ-$Al_2O_3/SrTiO_3$. *Nat. Commun.* **2013**, *4*, No. 1371.
(27) Yang, X.; Su, H.; Wu, G. Orbital-Adapted Electronic Structure and Anisotropic Transport in γ−$Al_2O_3/SrTiO_3$ Heterostructure. *Phys. Rev. Mater.* **2020**, *4*, No. 016001.
(28) Lei, S.; Lin, J.; Jia, Y.; Gray, M.; Topp, A.; Farahi, G.; Klemenz, S.; Gao, T.; Rodolakis, F.; McChesney, J. L.; Ast, C. R.; Yazdani, A.; Burch, K. S.; Wu, S.; Ong, N. P.; Schoop, L. M. High Mobility in a van Der Waals Layered Antiferromagnetic Metal. *Sci. Adv.* **2020**, *6*, No. eaay6407.
(29) Bonaccorso, F.; Sun, Z.; Hasan, T.; Ferrari, A. C. Graphene Photonics and Optoelectronics. *Nat. Photonics* **2010**, *4*, 611−622.
(30) Qiu, Y.; Zhang, B.; Yang, J.; Gao, H.; Li, S.; Wang, L.; Wu, P.; Su, Y.; Zhao, Y.; Feng, J.; Jiang, L.; Wu, Y. Wafer-Scale Integration of Stretchable Semiconducting Polymer Microstructures via Capillary Gradient. *Nat. Commun.* **2021**, *12*, No. 7038.
(31) Lin, L.; Li, J.; Yuan, Q.; Li, Q.; Zhang, J.; Sun, L.; Rui, D.; Chen, Z.; Jia, K.; Wang, M.; Zhang, Y.; Rummeli, M. H.; Kang, N.; Xu, H. Q.; Ding, F.; Peng, H.; Liu, Z. Nitrogen Cluster Doping for High-Mobility/Conductivity Graphene Films with Millimeter-Sized Domains. *Sci. Adv.* **2019**, *5*, No. eaaw8337.

https://doi.org/10.1021/acsami.3c03603
ACS Appl. Mater. Interfaces 2023, 15, 36866−36876

(32) Kagan, C. R.; Murray, C. B. Charge Transport in Strongly Coupled Quantum Dot Solids. *Nat. Nanotechnol.* **2015**, *10*, 1013−1026.
(33) Singh, R.; Kang, H.; Shin, H.; Park, J. Y.; Seo, H. Highly Transparent Conducting Two-Dimensional Electron Gas Channel in Ultrathin Heterostructures for Flexible Optoelectronic Device Applications. *Appl. Surf. Sci.* **2022**, *580*, No. 152266.
(34) Lee, S. Y.; Kim, J.; Park, A.; Park, J.; Seo, H. Creation of a Short-Range Ordered Two-Dimensional Electron Gas Channel in Al_2O_3/In_2O_3 Interfaces. *ACS Nano* **2017**, *11*, 6040−6047.
(35) Lee, H. J.; Moon, T.; Hyun, S. D.; Kang, S.; Hwang, C. S. Characterization of a 2D Electron Gas at the Interface of Atomic-Layer Deposited Al_2O_3/ZnO Thin Films for a Field-Effect Transistor. *Adv. Electron. Mater.* **2021**, *7*, No. 2000876.
(36) Lee, Y. A.; Kim, J.; Lee, S. Y.; Park, J.; Seo, H. Creation of a Two-Dimensional Conducting Path Based on the Engineering Oxidation State of WO_3 with Al_2O_3 at the Interface. *Appl. Surf. Sci.* **2019**, *481*, 1011−1017.
(37) Park, J.; Eom, H.; Kim, S. H.; Seok, T. J.; Park, T. J.; Lee, S. W.; Shong, B. Chemical Mechanism of Formation of Two-Dimensional Electron Gas at the Al_2O_3/TiO_2 Interface by Atomic Layer Deposition. *Mater. Today Adv.* **2021**, *12*, No. 100195.
(38) Seok, T. J.; Liu, Y.; Choi, J. H.; Kim, H. J.; Kim, D. H.; Kim, S. M.; Jang, J. H.; Cho, D. Y.; Lee, S. W.; Park, T. J. In Situ Observation of Two-Dimensional Electron Gas Creation at the Interface of an Atomic Layer-Deposited Al_2O_3/TiO_2 Thin-Film Heterostructure. *Chem. Mater.* **2020**, *32*, 7662−7669.
(39) Zhu, Z.; Suzuki, M.; Nagashima, K.; Yoshida, H.; Kanai, M.; Meng, G.; Anzai, H.; Zhuge, F.; He, Y.; Boudot, M.; Takeda, S.; Yanagida, T. Rational Concept for Reducing Growth Temperature in Vapor−Liquid−Solid Process of Metal Oxide Nanowires. *Nano Lett.* **2016**, *16*, 7495−7502.
(40) Zhu, Z.; Yasui, T.; Liu, Q.; Nagashima, K.; Takahashi, T.; Shimada, T.; Yanagida, T.; Baba, Y. Fabrication of a Robust In_2O_3 Nanolines FET Device as a Biosensor Platform. *Micromachines* **2021**, *12*, No. 642.
(41) Anzai, H.; Suzuki, M.; Nagashima, K.; Kanai, M.; Zhu, Z.; He, Y.; Boudot, M.; Zhang, G.; Takahashi, T.; Kanemoto, K.; Seki, T.; Shibata, N.; Yanagida, T. True Vapor−Liquid−Solid Process Suppresses Unintentional Carrier Doping of Single Crystalline Metal Oxide Nanowires. *Nano Lett.* **2017**, *17*, 4698−4705.
(42) Liu, Q.; Yasui, T.; Nagashima, K.; Yanagida, T.; Horiuchi, M.; Zhu, Z.; Takahashi, H.; Shimada, T.; Arima, A.; Baba, Y. Photolithographically Constructed Single ZnO Nanowire Device and Its Ultraviolet Photoresponse. *Anal. Sci.* **2020**, *36*, 1125−1129.
(43) Wang, S.; An, Y.; Feng, D.; Wu, Z.; Liu, J. The Local Structure, Magnetic, and Transport Properties of Cr-Doped In_2O_3 Films. *J. Appl. Phys.* **2013**, *113*, No. 153901.
(44) Shannon, R. D.; Prewitt, C. T. Effective Ionic Radii in Oxides and Fluorides. *Acta Crystallogr., Sect. B: Struct. Crystallogr. Cryst. Chem.* **1969**, *25*, 925−946.
(45) Khan, A.; Rahman, F.; Nongjai, R.; Asokan, K. Structural, Optical and Electrical Transport Properties of Sn Doped In_2O_3. *Solid State Sci.* **2020**, *109*, No. 106436.
(46) Sun, L.; Li, R.; Zhan, W.; Yuan, Y.; Wang, X.; Han, X.; Zhao, Y. Double-Shelled Hollow Rods Assembled from Nitrogen/Sulfur-Codoped Carbon Coated Indium Oxide Nanoparticles as Excellent Photocatalysts. *Nat. Commun.* **2019**, *10*, No. 2270.
(47) Shen, C.; Sun, K.; Zhang, Z.; Rui, N.; Jia, X.; Mei, D.; Liu, C. Highly Active Ir/In_2O_3 Catalysts for Selective Hydrogenation of CO_2 to Methanol: Experimental and Theoretical Studies. *ACS Catal.* **2021**, *11*, 4036−4046.
(48) Guo, R.; Li, Q.; Zheng, Y.; Lei, B.; Sun, H.; Hu, Z.; Zhang, J.; Wang, L.; Longhi, E.; Barlow, S.; Marder, S. R.; Wang, J.; Chen, W. Degenerate Electron-Doping in Two-Dimensional Tungsten Diselenide with a Dimeric Organometallic Reductant. *Mater. Today* **2019**, *30*, 26−33.
(49) Zhu, Q.; Xie, C.; Li, H.; Yang, C.; Zhang, S.; Zeng, D. Selectively Enhanced UV and NIR Photoluminescence from a Degenerate ZnO Nanorod Array Film. *J. Mater. Chem. C* **2014**, *2*, 4566−4580.
(50) Dimoulas, A.; Zekentes, K.; Androulidaki, M.; Kornelios, N.; Michelakis, C.; Hatzopoulos, Z. Degenerate Electron Gas Effects in the Modulation Spectroscopy of Pseudomorphic $Al_{0.32}Ga_{0.68}As/In_{0.15}Ga_{0.85}As/GaAs$ High Electron Mobility Transistor Structures. *Appl. Phys. Lett.* **1993**, *63*, 1417−1419.
(51) Jena, D.; Gossard, A. C.; Mishra, U. K. Dislocation Scattering in a Two-Dimensional Electron Gas. *Appl. Phys. Lett.* **2000**, *76*, 1707−1709.
(52) Jiang, H. W.; Johnson, C. E.; Wang, K. L. Giant Negative Magnetoresistance of a Degenerate Two-Dimensional Electron Gas in the Variable-Range-Hopping Regime. *Phys. Rev. B* **1992**, *46*, 12830−12833.
(53) Fu, Q.; Wagner, T.; Rühle, M. Hydroxylated α-Al_2O_3 (0001) Surfaces and Metal/α-Al_2O_3 (0001) Interfaces. *Surf. Sci.* **2006**, *600*, 4870−4877.
(54) Kim, J. S.; Joo, M. K.; Piao, X. M.; Ahn, S. E.; Choi, Y. H.; Jang, H. K.; Kim, G. T. Plasma Treatment Effect on Charge Carrier Concentrations and Surface Traps in A-InGaZnO Thin-Film Transistors. *J. Appl. Phys.* **2014**, *115*, No. 114503.
(55) Jin Fan, H.; Knez, M.; Scholz, R.; Nielsch, K.; Pippel, E.; Hesse, D.; Zacharias, M.; Gösele, U. Monocrystalline Spinel Nanotube Fabrication Based on the Kirkendall Effect. *Nat. Mater.* **2006**, *5*, 627−631.
(56) Ren, Y.; Chim, W. K.; Chiam, S. Y.; Huang, J. Q.; Pi, C.; Pan, J. S. Formation of Nickel Oxide Nanotubes with Uniform Wall Thickness by Low-Temperature Thermal Oxidation Through Understanding the Limiting Effect of Vacancy Diffusion and the Kirkendall Phenomenon. *Adv. Funct. Mater.* **2010**, *20*, 3336−3342.
(57) Zolotaryov, A.; Goetze, S.; Zierold, R.; Novikov, D.; Birajdar, B.; Hesse, D.; Nielsch, K. Temperature-Dependent Solid-State Reactions With and Without Kirkendall Effect in Al_2O_3/ZnO, Fe_2O_3/ZnO, and Co_XO_Y/ZnO Oxide Thin Film Systems. *Adv. Eng. Mater.* **2010**, *12*, 509−516.
(58) Sudakar, C.; Dixit, A.; Kumar, S.; Sahana, M. B.; Lawes, G.; Naik, R.; Naik, V. M. Coexistence of Anion and Cation Vacancy Defects in Vacuum-Annealed In_2O_3 Thin Films. *Scr. Mater.* **2010**, *62*, 63−66.
(59) Cao, H.; Xing, P.; Yao, D.; Wu, P. Annealing Temperature Dependent Non-Monotonic D0 Ferromagnetism in Pristine In_2O_3 Nanoparticles. *J. Magn. Magn. Mater.* **2017**, *429*, 69−73.
(60) Wiranwetchayan, O.; Ruankham, P.; Promnopas, W.; Choopun, S.; Singjai, P.; Chaipanich, A.; Thongtem, S. Effect of Nanoporous In_2O_3 Film Fabricated on TiO_2-In_2O_3 Photoanode for Photovoltaic Performance via a Sparking Method. *J. Solid State Electrochem.* **2018**, *22*, 2531−2543.
(61) Gan, J.; Lu, X.; Wu, J.; Xie, S.; Zhai, T.; Yu, M.; Zhang, Z.; Mao, Y.; Wang, S. C. I.; Shen, Y.; Tong, Y. Oxygen Vacancies Promoting Photoelectrochemical Performance of In_2O_3 Nanocubes. *Sci. Rep.* **2013**, *3*, No. 1021.

https://doi.org/10.1021/acsami.3c03603
ACS Appl. Mater. Interfaces 2023, 15, 36866−36876